

1 **Early warnings and missed alarms for abrupt monsoon transitions**

2
3 **Authors:** Zoë A. Thomas^{1,2*}, Frank Kwasniok³, Chris A. Boulton², Peter M. Cox³, Richard
4 T. Jones², Timothy M. Lenton², Chris S.M. Turney¹

5 6 **Affiliations**

7 ¹Climate Change Research Centre and School of Biological, Earth & Environmental
8 Sciences, University of New South Wales, Sydney, NSW 2052, Australia

9 ²College of Life and Environmental Science, University of Exeter, Exeter, EX4 4RJ, UK

10 ³College of Engineering, Mathematics and Physical Sciences, University of Exeter, Exeter,
11 EX4 4QF, UK

12 * E-mail: z.thomas@unsw.edu.au

13 14 **Abstract**

15 Palaeo-records from China demonstrate that the East Asian Summer Monsoon (EASM) is
16 dominated by abrupt and large magnitude monsoon shifts on millennial timescales,
17 switching between periods of high and weak monsoon rains. It has been hypothesised that
18 over these timescales, the EASM exhibits two stable states with bifurcation-type tipping
19 points between them. Here we test this hypothesis by looking for early warning signals of
20 past bifurcations in speleothem $\delta^{18}\text{O}$ records from Sanbao Cave and Hulu Cave, China,
21 spanning the penultimate glacial cycle. We find that although there are increases in both
22 autocorrelation and variance preceding some of the monsoon transitions during this period,
23 it is only immediately prior to the abrupt monsoon shift at the penultimate deglaciation
24 (Termination II) that statistically significant increases are detected. To supplement our data
25 analysis, we produce and analyse multiple model simulations that we derive from these

26 data. We find hysteresis behaviour in our model simulations with transitions directly forced
27 by solar insolation. However, signals of critical slowing down, which occur on the approach
28 to a bifurcation, are only detectable in the model simulations when the change in system
29 stability is sufficiently slow to be detected by the sampling resolution of the dataset. This
30 raises the possibility that the early warning ‘alarms’ were missed in the speleothem data
31 over the period 224-150 kyr and it was only at the monsoon termination that the change in
32 the system stability was sufficiently slow to detect early warning signals.

33

34 **Keywords: Speleothem, monsoon, bifurcation, early warning signals, tipping point**

35

36 **1.1 Introduction**

37 The Asian Summer Monsoon directly influences over 60% of the world’s population (Wu et
38 al., 2012) and yet the drivers of past and future variability remain highly uncertain
39 (Levermann et al., 2009; Zickfeld et al., 2005). Evidence from radiometrically-dated East
40 Asian speleothem records of past monsoon behaviour (Yuan et al., 2004) suggests that on
41 millennial timescales, the EASM is driven by a 23 kyr precession cycle (Kutzbach, 1981;
42 Wang et al., 2008), but also influenced by feedbacks in sea surface temperatures and
43 changing boundary conditions including Northern Hemisphere ice volume (An, 2000; Sun
44 et al., 2015). The abrupt nature of the monsoon behaviour (interpreted as a precipitation
45 proxy from $\delta^{18}\text{O}$ values from Chinese speleothem records; see Section 1.4) in comparison to
46 the sinusoidal insolation forcing strongly implies that this response is non-linear (Figure 1);
47 whilst Northern Hemisphere Summer Insolation (NHSI) follows a quasi-sinusoidal cycle,
48 the $\delta^{18}\text{O}$ profile in speleothems exhibits a step function, suggesting the presence of
49 threshold behaviour in the monsoon system (Schewe et al., 2012). Though the vulnerability
50 of society has clearly changed, future abrupt monsoon shifts, whether caused by orbital or

51 anthropogenic forcing, are likely to have major devastating societal impacts (Donges et al.,
52 2015).

53

54

55 **Figure 1:** (a) Northern Hemisphere Summer Insolation (NHSI) at June 30°N (Berger &
56 Loutre, 1991) (grey), $\delta^{18}\text{O}$ speleothem data from Sanbao Cave (Wang et al., 2008) (dark
57 blue), (b) $\delta^{18}\text{O}$ speleothem data from Hulu Cave (Wang et al., 2001); speleothem MSH
58 (red), MSP (blue) and MSX (yellow), (c) $\delta^{18}\text{O}$ per mille benthic carbonate (Lisiecki &
59 Raymo, 2005) (proxy for global ice volume) (purple).

60

61

62 A minimum conceptual model of the East Asian Summer Monsoon developed by Zickfeld
63 et al. (2005), stripped down by Levermann et al. (2009) and updated by Schewe et al.
64 (2012), shows a non-linear solution structure with thresholds for switching a monsoon
65 system between ‘on’ or ‘off’ states that can be defined in terms of atmospheric humidity –
66 in particular, atmospheric specific humidity over the adjacent ocean (Schewe et al., 2012).
67 Critically, if specific humidity levels pass below a certain threshold, for instance, as a result
68 of reduced sea surface temperatures, insufficient latent heat is produced in the atmospheric
69 column and the monsoon fails. This moisture-advection feedback allows for the existence of
70 two stable states, separated by a saddle-node bifurcation (Zickfeld et al., 2005) (although
71 interestingly, the conceptual models of Levermann et al. (2009) and Schewe et al. (2012)
72 are characterised by a single bifurcation point for switching ‘off’ the monsoon and an
73 arbitrary threshold to switch it back ‘on’). Crucially, the presence of a critical threshold at
74 the transition between the strong and weak regimes of the EASM means that early warning

75 signals related to ‘critical slowing down’ (Dakos et al., 2008; Lenton et al., 2012) could be
76 detectable in suitable proxy records.

77

78 The aim of this study was twofold: (1) to test whether shifts in the EASM during the
79 penultimate glacial cycle (Marine Isotope Stage 6) are consistent with bifurcational tipping
80 points, and (2) if so, is it possible to detect associated early warning signals. To achieve
81 this, we analyse two $\delta^{18}\text{O}$ speleothem records from China, and construct a simple model
82 that we derive directly from this data to test whether we can detect early warning signals of
83 these transitions.

84

85 **1.2 Detecting early warning signals**

86 We perform ‘tipping point analysis’ on both the $\delta^{18}\text{O}$ speleothem records and on multiple
87 simulations derived from our model. This analysis aims to find early warning signs of
88 impending tipping points that are characterised by a bifurcation (rather than a noise-induced
89 tipping, induced by stochastic fluctuations with no change in forcing control, or rate-
90 dependent tipping, where a system fails to track a continuously changing quasi-static
91 attractor e.g. (Ashwin et al., 2012)). These tipping points can be mathematically detected by
92 looking at the pattern of fluctuations in the short-term trends of a time-series before the
93 transition takes place. A phenomenon called ‘critical slowing down’ occurs on the approach
94 to a tipping point, whereby the system takes longer to recover from small perturbations
95 (Kleinen et al., 2003; Held & Kleinen, 2004; Dakos et al., 2008). This longer recovery rate
96 causes the intrinsic rates of change in the system to decrease, which is detected as a short-
97 term increase in the autocorrelation or ‘memory’ of the time-series (Ives, 1995), often
98 accompanied by an increasing trend in variance (Lenton et al., 2012). It has been
99 theoretically established that autocorrelation and variance should both increase together

100 (Ditlevsen & Johnsen, 2010; Thompson & Sieber, 2011). Importantly, it is the increasing
101 trend, rather than the absolute values of the autocorrelation and variance that indicate
102 critical slowing down. Detecting the phenomenon of critical slowing down relies on a
103 timescale separation, whereby the timescale forcing the system is much slower than the
104 timescale of the system's internal dynamics, which is in turn much longer than the
105 frequency of data sampling the system (Held & Kleinen, 2004). Importantly, the monsoon
106 transitions span hundreds of years (corresponding to several data points), meeting the
107 criterion that the frequency of sampling is higher than the timescale of the transition of the
108 system.

109

110 **1.3 Missed alarms**

111 Although efforts have been taken to reduce the chances of type I (incorrect rejection of a
112 true null hypothesis, otherwise known as a 'false positive') and type II (failure to reject a
113 false null hypothesis, or 'false negative') errors by correct pre-processing of data e.g.
114 (Lenton, 2011), totally eradicating the chances of false positive and false negative results
115 remains a challenge (Scheffer, 2010; Lenton et al., 2012; Dakos et al., 2014). Type II errors
116 or 'missed alarms', as discussed in Lenton (2011), may occur when internal noise levels are
117 such that the system is 'tipped' into a different state prior to reaching the bifurcation point,
118 precluding the detection of early warning signals. Type I errors are potentially easier to
119 guard against by employing strict protocols by which to reject a null hypothesis.

120

121 **1.4 Using speleothem $\delta^{18}\text{O}$ data as a proxy of past monsoon strength**

122 Highly-resolved ($\sim 10^2$ years) and precisely dated speleothem records of past monsoonal
123 variability are well placed to test for early warning signals. The use of speleothem-based
124 proxies to reconstruct patterns of palaeo-monsoon changes has increased rapidly over recent

125 decades with the development of efficient sampling and dating techniques. However, there
126 is currently some debate surrounding the climatic interpretation of Chinese speleothem $\delta^{18}\text{O}$
127 records (An et al., 2015), which can be influenced by competing factors that affect isotope
128 fractionation. The oxygen isotopic composition of speleothem calcite is widely used to
129 reconstruct palaeohydrological variations due to the premise that speleothem calcite $\delta^{18}\text{O}$
130 records the stable isotopic content of precipitation, which has been shown to be inversely
131 correlated with precipitation amount (Dansgaard, 1964; Lee & Swann, 2010), a relationship
132 known as the ‘amount effect’. Although the $\delta^{18}\text{O}$ of speleothem calcite in China has
133 traditionally been used as a proxy for the ‘amount effect’ (Cheng et al., 2006; Wang et al.,
134 2008; Cheng et al., 2009; Wang et al., 2009), this has been challenged by other palaeo-
135 wetness proxies, notably Maher (2008), who argues that speleothems may be influenced by
136 changes in rainfall source rather than amount. The influence of the Indian Monsoon has also
137 been proposed as an alternative cause for abrupt monsoon variations in China (Liu et al.,
138 2006; Pausata et al., 2011), though this has since been disputed (Wang & Chen, 2012; Liu
139 et al., 2014). Importantly, however, robust replications of the same $\delta^{18}\text{O}$ trends in
140 speleothem records across the wider region suggest they principally represent changes in the
141 delivery of precipitation $\delta^{18}\text{O}$ associated with the EASM (Cheng et al., 2009; Cheng et al.,
142 2012; Li et al., 2013; Duan et al., 2014; Liu et al., 2014; Baker et al., 2015).

143

144 Specific data requirements are necessary to search for early warning signs of tipping points
145 in climate systems; not only does the data have to represent a measure of climate, it also
146 must be of a sufficient length and resolution to enable the detection of critical slowing
147 down. In addition, since time series analysis methods require interpolation to equidistant
148 data points, a relative constant density of data points is important, so that the interpolation
149 does not skew the data. The speleothem $\delta^{18}\text{O}$ records that we have selected fulfil these

150 criteria, as described in more detail in section 2.1.

151

152

153 **2. Methods**

154 **2.1 Data selection**

155 We used the Chinese speleothem sequences from Sanbao Cave (31°40'N, 110°26'E) (Wang
156 et al., 2008), and Hulu Cave (32°30'N, 119°10'E) (Wang et al., 2001) to search for early
157 warning signals. Sanbao Cave (speleothem SB11) and Hulu Cave (speleothem MSP) have
158 two of the highest resolution chronologies in the time period of interest, with a relatively
159 constant density of data points, providing some of the best records of Quaternary-scale
160 monsoonal variation. Speleothem $\delta^{18}\text{O}$ records offer considerable advantages for
161 investigating past changes in the EASM: their long duration (10^3 - 10^4 years), high-resolution
162 (~ 100 years) and precise and absolute-dated chronologies (typically 1 kyr at 1σ), make
163 them ideal for time series analysis. Speleothem SB11 has one of the longest, continuous
164 $\delta^{18}\text{O}$ records in China, and is the only series spanning an entire glacial cycle without using a
165 spliced record (Wang et al. 2008). Speleothem MSP has a comparable resolution and
166 density to SB11, though is significantly shorter. Crucially, the cave systems lie within two
167 regionally distinct areas (Figure 2), indicating that parallel changes in $\delta^{18}\text{O}$ cannot be
168 explained by local effects.

169

170

171 **Figure 2** Map showing the location of Sanbao and Hulu caves.

172

173

174 **2.2 Searching for bimodality**

175 A visual inspection of a histogram of the speleothem $\delta^{18}\text{O}$ data was initially undertaken to
176 determine whether the data are likely to be bimodal. We then applied a Dip-test of
177 unimodality (Hartigan & Hartigan, 1985) to test whether our data is bimodal. To investigate
178 further the dynamical origin of the modality of our data we applied non-stationary potential
179 analysis (Kwasniok, 2013; Kwasniok, 2015). A non-stationary potential model (discussed in
180 more detail in section 2.4) was fitted, modulated by the solar forcing (NHSI June
181 30°N), covering the possibility of directly forced transitions as well as noise-induced
182 transitions with or without stochastic resonance.

183

184

185 **2.3 Tipping point analysis**

186 A search for early warning signals of a bifurcation at each monsoon transition was carried
187 out between 224-128 kyr of the Sanbao Cave and Hulu Cave speleothem records. Stable
188 periods of the Sanbao Cave $\delta^{18}\text{O}$ record (e.g. excluding the abrupt transitions) were initially
189 identified visually and confirmed by subsequent analysis using a climate regime shift
190 detection method described by Rodionov (2004). Data pre-processing involved removal of
191 long term trends using a Gaussian kernel smoothing filter and interpolation to ensure that
192 the data is equidistant (a necessary assumption for time-series analysis), before the trends in
193 autocorrelation and variance (using the R functions *acf()* and *var()* respectively) are
194 measured over a sliding window of half the data length (Lenton et al., 2012). The density of
195 data points over time do not change significantly in either record and thus the observed
196 trends in autocorrelation are not an artefact of the data interpolation. The smoothing
197 bandwidth was chosen such that long-term trends were removed without overfitting the
198 data. A sensitivity analysis was undertaken by varying the size of the smoothing bandwidth
199 and sliding window to ensure the results were robust over a range of parameter choices. The

200 nonparametric Kendall's tau rank correlation coefficient was applied (Kendall, 1948; Dakos
201 et al., 2008) to test for statistical dependence for a sequence of measurements against time,
202 varying between +1 and -1, describing the sign and strength of any trends in autocorrelation
203 and variance.

204

205 **2.3.1 Assessing significance**

206 The results were tested against surrogate time series to ascertain the significance level of the
207 results found, based on the null hypothesis that the data are generated by a stationary
208 Gaussian linear stochastic process. This method for assessing significance of the results is
209 based on Dakos et al. (2012a). The surrogate time series were generated by randomising the
210 original data over 1000 permutations, which is sufficient to adequately estimate the
211 probability distribution of the null model, and destroys the memory while retaining the
212 amplitude distribution of the original time series. The autocorrelation and variance for the
213 original and each of the surrogate time series was computed, and the statistical significance
214 obtained for the original data by comparing against the frequency distribution of the trend
215 statistic (Kendall tau values of autocorrelation and variance) from the surrogate data.

216 Importantly, the Kendall tau values are calculated relatively, thus when the autocorrelation
217 is destroyed by randomisation, the null model distribution does not change. Higher Kendall
218 tau values indicate a stronger increasing trend. The 90th and 95th percentiles provided the
219 90% and 95% rejection thresholds (or p-values of 0.1 and 0.05) respectively. According to
220 the fluctuation-dissipation theorem (Ditlevsen & Johnsen, 2010), both autocorrelation and
221 variance should increase together on the approach to a bifurcation. Previous tipping point
222 literature has often used a visual increasing trend of autocorrelation and variance as
223 indicators of critical slowing down. Although using surrogate data allows a quantitative
224 assessment of the significance of the results, there is no consensus on what significance

225 level is necessary to declare the presence of precursors of critical slowing down. To
226 guard against type I errors, we determine for this study that ‘statistically significant’ early
227 warning indicators occur with increases in both autocorrelation and variance with p-values
228 < 0.1 . We have chosen this benchmark in line with previous studies using a similar null
229 model that have described results with $p < 0.1$ as ‘robust’ (Dakos et al., 2008; Boulton &
230 Lenton, 2015).

231

232 **2.4 Non-stationary potential analysis**

233 To supplement the analysis of the speleothem records and help interpret the results, a simple
234 stochastic model derived directly from the Sanabo cave $\delta^{18}\text{O}$ data was constructed. Non-
235 stationary potential analysis (Kwasniok, 2013; Kwasniok, 2015) is a method for deriving
236 from time series data a simple dynamical model which is modulated by external factors,
237 here solar insolation. The technique allows extraction of basic dynamical mechanisms and
238 to distinguish between competing dynamical explanations.

239

240 The dynamics of the monsoon system are conceptually described as noise-driven motion in
241 a time- dependent potential landscape. The governing equation is a one-dimensional non-
242 stationary effective Langevin equation:

$$243 \quad \dot{x} = -V'(x;t) + \sigma\eta \quad (1)$$

244 The model variable x is identified with the speleothem $\delta^{18}\text{O}$ record, which is a proxy for
245 monsoon strength. The potential function $V(x;t)$ describes the force field governing the
246 monsoon system. η is a white Gaussian noise process with zero mean and unit variance, and
247 σ is the amplitude of the stochastic forcing. The noise term is meant to account for the
248 influence of unresolved temporal and spatial scales. The potential landscape is time-
249 dependent, modulated by the solar insolation:

250
$$V(x; t) = U(x) + \gamma I(t)x \quad (2)$$

251 The time-independent part of the potential is modelled by a fourth-order polynomial,
252 allowing for possible bi-stability (Kwasniok & Lohmann, 2009):

253
$$U(x) = \sum_{i=1}^4 a_i x^i \quad (3)$$

254 $I(t)$ is the insolation forcing and γ is a coupling parameter. The modulation of the potential
255 is only in the linear term, that is, the time-independent potential system is subject to the
256 scaled insolation forcing $\gamma I(t)$. The insolation is represented as a superposition of three main
257 frequencies as

258
$$I(t) = \alpha_0 + \sum_{i=1}^3 [\alpha_i \cos(2\pi t/T_i) + \beta_i \sin(2\pi t/T_i)] \quad (4)$$

259 with time t measured in kyr. The expansion coefficients α_i and β_i are determined by least-
260 squares regression on the insolation time series over the time interval of the speleothem
261 record. The periods T_i are found by a search over a grid with mesh size 0.5kyr. They are, in
262 order of decreasing contribution $\alpha_i^2 + \beta_i^2$, $T_1 = 23\text{kyr}$, $T_2 = 19.5\text{kyr}$ and $T_3 = 42\text{kyr}$. This
263 yields an excellent approximation of the insolation time series over the time interval under
264 consideration here.

265

266 The potential model covers and allows us to distinguish between two possible scenarios: (i)
267 In the bifurcation scenario, the monsoon transitions are directly forced by the insolation,
268 where two states are stable in turn, one at a time. This corresponds to a fairly large value of
269 γ . (ii) Alternatively, two stable states could be available at all times with noise-induced
270 switching between them. This is realised with $\gamma = 0$, giving a stationary potential. The
271 height of the potential barrier separating the two states could be modulated by the
272 insolation, possibly giving rise to a stochastic resonance which would explain the high

273 degree of coherence between the solar forcing and the monsoon transitions. The latter
274 variant would correspond to a small but non-zero value of γ .

275

276 The shape of the potential, as well as the noise level, are estimated directly from the
277 speleothem data according to the maximum likelihood principle. We take a two-step
278 approach, combining non-stationary probability density modelling (Kwasniok, 2013) and
279 dynamical modeling (Kwasniok, 2015). The shape of the potential is estimated from the
280 probability density of the data. The quasi-stationary probability density of the potential
281 model is

$$p(x; t) = Z^{-1}(t) \exp[-2V(x; t)/\sigma^2] \quad (5)$$

282

283 with a time-dependent normalisation constant $Z(t)$. The coefficients a_i and the coupling
284 constant γ are estimated by maximising the likelihood function

$$L(x_1, \dots, x_N) = \prod_{i=1}^N p(x_n; t_n) \quad (6)$$

285

286 as described in Kwasniok (2013). The size of the data set is $N=1288$. This leaves the noise
287 level undetermined as a scaling of the potential with a constant c and a simultaneous scaling
288 of the noise variance with c keeps the quasi-stationary probability density unchanged. We
289 set $\sigma = 1$ for the (preliminary) estimation of a_i and γ . The noise level is now determined
290 from the dynamical likelihood function based on the time evolution of the system
291 (Kwasniok, 2015). The Langevin equation is discretised according to the Euler-Maruyama
292 scheme:

$$x_{n+1} = x_n - \delta t_n V'(x_n; t_n) + \sqrt{\delta t_n} \sigma \eta_n \quad (7)$$

293

294 The sampling interval of the data is $\delta t_n = t_{n+1} - t_n$. The log-likelihood function of the data
295 is

$$l(x_1, \dots, x_N | x_0) = -\frac{N}{2} \log 2\pi - N \log \sigma - \frac{1}{2} \sum_{n=0}^{N-1} \left(\log \delta t_n + \frac{[x_{n+1} - x_n + \delta t_n V'(x_n; t_n)]^2}{\delta t_n \sigma^2} \right) \quad (8)$$

296

297 The scaling constant c is searched on a grid with mesh size 0.01 and the log-likelihood
 298 maximised, giving the final estimates of all parameters. Both estimation procedures are
 299 applied directly to the unevenly sampled data without any prior interpolation. We remark
 300 that the more natural and simpler approach of estimating all parameters simultaneously
 301 from the dynamical likelihood (Kwasniok, 2015) here yields a negative leading-order
 302 coefficient a_4 and thus the model cannot be integrated over a longer time period without the
 303 trajectory escaping to infinity. This possibly points at limitations in the degree of validity of
 304 the one-dimensional potential model. Palaeoclimatic records reflect a multitude of complex
 305 processes and any model as simple as equation (1) cannot be expected to be more than a
 306 skeleton model used to pinpoint and contrast basic dynamical mechanisms. The described
 307 estimation method guarantees a positive leading-order coefficient a_4 and therefore a
 308 globally stable model.

309

310 It has been suggested that the EASM system responds specifically to 21st July insolation at
 311 65°N with a “near-zero phase lag” (Ruddiman, 2006). However, given that EASM
 312 development is affected by both remote and local insolation forcing (Liu et al., 2006), we
 313 use an insolation latitude local to the Sanbao Cave record, consistent with earlier studies
 314 from this and other speleothem sequences (Wang et al., 2001). Since the monthly maximum
 315 insolation shifts in time with respect to the precession parameter, the 30°N June insolation
 316 was used, though we acknowledge that the insolation changes of 65°N 21 July as used by
 317 Wang et al. (2008) are similar with regard to the timing of maxima and minima. Crucially,
 318 immediately prior to Termination II, the Chinese speleothem data (including Sanbao Cave)
 319 record a ‘Weak Monsoon Interval’ between 135.5 and 129 kyr (Cheng et al., 2009),

320 suggesting a lag of approximately 6.5 kyrs following Northern Hemisphere summer
321 insolation (Figure 1).
322
323 Having derived a model from the data, 100 realisations were analysed to test whether early
324 warning signals could be detected in the model output, using the methods set out in section
325 2.3. We initially chose the sampling resolution of the model outputs to be comparable to the
326 speleothem data (10^2 years). Subsequently, the model was manipulated by changing both
327 the noise level and the sampling resolution in order to explore the effect of these on the
328 early warning signals in a hypothetical scenario. To enable a straightforward comparison of
329 the rate of forcing and the sampling resolution we linearized the solar insolation using the
330 minimum and maximum values of the solar insolation over the time span of the model (224-
331 128 kyr). This approach was preferred rather than using a sinusoidal forcing since early
332 warning signals are known to work most effectively when there is a constant increase in the
333 forcing. To detrend the time series data, we ran the model without any external noise
334 forcing to obtain the equilibrium solution to the system, which we then subtracted from the
335 time series, which did include noise. In addition, we manipulated the noise level of the
336 model by altering the amplitude of the stochastic forcing (σ in Equation 1). The time step in
337 the series was reduced so that 6000 time points were available prior to the bifurcation and to
338 ensure no data from beyond the tipping point was included in the analysis. Sampling the
339 same time series at different resolutions allowed us to explore the effect of this on the early
340 warning signals. When comparing early warning signals for differing sample steps and
341 noise levels, the same iteration of the model was used to enable a direct comparison.

342

343 **3. Results**

344 **3.1 Bimodality and non-stationary potential modelling**

345 A histogram of $\delta^{18}\text{O}$ values suggests there are two modes in the EASM between 224-128
346 kyr, as displayed by the double peak structure in Figure 3a, supporting a number of studies
347 that observe bimodality in tropical monsoon systems (Zickfeld et al., 2005; Schewe et al.,
348 2012). We also apply a Dip-test of unimodality (Hartigan & Hartigan, 1985) and find that
349 our null hypothesis of unimodality is rejected ($D=0.018$, $p=0.0063$) and thus our data is at
350 least bimodal. To investigate further the dynamical origin of this bimodality we
351 applied non-stationary potential analysis (Kwasniok, 2013; Kwasniok, 2015). This showed
352 a bi-stable structure to the EASM with hysteresis (Figure 3b, c), suggesting that abrupt
353 monsoon transitions may involve underlying bifurcations. The monsoon transitions appear
354 to be predominantly directly forced by the insolation. There is a phase in the middle of the
355 transition cycle between the extrema of the insolation where two stable states are available
356 at the same time but this phase is too short for noise-induced switches to play a significant
357 role.

358

359 We are able to clearly refute from the speleothem data the scenario of noise-induced
360 switching between two simultaneously available states in favour of the bifurcation scenario.
361 When fitting a model without solar insolation forcing (that is, $\gamma = 0$) we obtain a stationary
362 potential with two deep wells and noise-driven switching between them. However, the pdf-
363 based log-likelihood of equation (6) is $l = -2149.1$ versus $l = -1943.2$ for the model with
364 insolation forcing and the dynamical log-likelihood of equation (8) is $l = -353.6$ versus $l = -$
365 346.6 . This provides very strong evidence for the bifurcation scenario; based on both
366 likelihood functions, both the Akaike and the Bayesian information criterion clearly prefer
367 the model with solar insolation forcing. The value of γ is fairly large and the stationary part
368 of the potential is not strongly bistable, as evidenced by the shape of the potential given in
369 Figure 3, ruling out the stochastic resonance scenario. The uncertainty in all parameters,

370 including the noise level, is very small, making our model estimation robust. We tried more
371 complicated models where also the higher-order terms in the potential are modulated by the
372 insolation rather than just the linear term or where the solar insolation enters nonlinearly
373 into the model; the gain in likelihood is found to be rather minor compared to the gain
374 achieved when adding the modulation in the linear term of the potential.

375

376

377 **Figure 3** (a) Histogram showing the probability density of the speleothem data aggregated
378 over 224-128 kyr, (b) Bifurcation diagram obtained from potential model analysis, showing
379 bi-stability and hysteresis. Solid black lines indicate stable states, dotted line unstable states,
380 and dashed vertical lines the jumps between the two stable branches. Coloured vertical lines
381 correspond to the insolation values for which the potential curve is shown in panel c; (c)
382 Shows how the shape of the potential well changes over one transition cycle (198-175 kyr)
383 (green long dash = 535 W/m², purple short dash = 531 W/m², blue solid = 490 W/m², red
384 dotted = 449 W/m²) (for more details see Figure 10).

385

386

387 **3.2 Tipping point analysis**

388 We applied tipping point analysis on the Sanbao Cave $\delta^{18}\text{O}$ record on each section of data
389 prior to a monsoon transition. Although autocorrelation and variance do increase prior to
390 some of the abrupt monsoon transitions (Figure 4), these increases are not consistent
391 through the entire record. Surrogate datasets used to test for significance of our results
392 showed that p-values associated with these increases are only <0.1 for both autocorrelation
393 and variance (Figure 5) in one instance. Although a visual increasing trend has been used in

394 previous literature as an indicator of critical slowing down, we choose more selective
395 criteria to guard against the possibility of false positives.

396

397

398 **Figure 4** a) $\delta^{18}\text{O}$ speleothem data from Sanbao Cave (SB11) (blue line) and NHSI at July
399 65°N (grey line). Grey hatched areas show the sections of data selected for tipping point
400 analysis. b) Autocorrelation and variance for each period prior to a transition.

401

402

403 **Figure 5** Histogram showing frequency distribution of Kendall tau values from 1000
404 realisations of a surrogate time series model (described in Section 2.3.1), for Sanbao Cave
405 (a, b) and Hulu Cave (c, d) $\delta^{18}\text{O}$ data. The grey dashed lines indicate the 90% ($p < 0.1$) and
406 95% ($p < 0.05$) significance level. Each coloured line denotes the Kendall tau values for
407 autocorrelation and variance, for each section of speleothem data analysed (red = 131-156
408 kyr; yellow = 166-177 kyr; purple = 180-189 kyr; green = 191-198 kyr; orange = 200-208
409 kyr; blue = 214-225 kyr).

410

411

412 The only section of data prior to a monsoon transition that sees p-values of < 0.1 for the
413 increases in both autocorrelation and variance is for the data spanning the period 150 to 129
414 kyr in the Sanbao Cave record, before Monsoon Termination II (Figure 6). We find that the
415 Kendall tau value for autocorrelation has a significance level of $p < 0.05$ and for variance a
416 significance level of $p < 0.1$ (Figure 5a and 5b). These proportional positive trends in both
417 autocorrelation and variance are consistent with critical slowing down on the approach to a
418 bifurcation (Ditlevsen & Johnsen, 2010).

419

420

421 **Figure 6** Tipping Point analysis on data from Sanbao Cave (Speleothem SB11) ($31^{\circ}40'N$,
422 $110^{\circ}26'E$). (a) Data was smoothed over an appropriate bandwidth (purple line) to produce
423 data residuals (b), and analysed over a sliding window (of size between the two grey
424 vertical lines). The grey vertical line at 131 ka BP indicates the tipping point, and the point
425 up to which the data is analysed. (d) AR(1) values and associated Kendall tau value, and (e)
426 displays the variance and associated Kendall tau value.

427

428 To test whether the signal is present in other EASM records, we undertook the same
429 analysis on a second speleothem sequence of comparable age (Figure 7). We find that
430 speleothem MSP from Hulu Cave ($32^{\circ}30'N$, $119^{\circ}10'E$) (Wang et al., 2001) displays a
431 comparable increase in autocorrelation and variance to speleothem SB11 from Sanbao
432 Cave, though these do display slightly lower p-values (Figure 5c and 5d).

433

434

435 **Figure 7** Tipping Point analysis on data from Hulu Cave (Speleothem MSP) ($32^{\circ}30' N$,
436 $119^{\circ}10' E$) (a) Data was smoothed over an appropriate bandwidth (purple line) to produce
437 data residuals (b), and analysed over a sliding window (of size between the two grey
438 vertical lines). The grey vertical line at 131 ka BP indicates the tipping point, and the point
439 up to which the data is analysed. (d) Autocorrelation values and associated Kendall tau
440 value, and (e) the variance and associated Kendall tau value.

441

442

443 Furthermore, a sensitivity analysis was performed (results shown for data preceding the
444 monsoon termination in both speleothem SB11 and MSP, Figure 8) to ensure that the results
445 are robust over a range of parameters by running repeats of the analysis with a range of
446 smoothing bandwidths used to detrend the original data (5-15% of the time series length)
447 and sliding window sizes in which indicators are estimated (25-75% of the time series
448 length). The colour contours show how the Kendall tau values change when using different
449 parameter choices; for the autocorrelation at Sanbao Cave the Kendall tau values are over
450 0.8 for the vast majority of smoothing bandwidth and sliding window sizes (Figure 8a),
451 indicating a robust analysis.

452

453

454 **Figure 8** Contour plots showing a range of window and bandwidth sizes for the analysis;
455 (a) Sanbao SB11 autocorrelation, (b) Sanbao SB11 variance, (c) Hulu MSP autocorrelation,
456 (d) Hulu MSP variance. Black stars indicate the parameters used for the analysis in Figures
457 6 and 7.

458

459

460 **3.3 Potential model simulations**

461 To help interpret these results we applied our potential model. In the model we find
462 transitions occur under direct solar insolation forcing when reaching the end of the stable
463 branches, explaining the high degree of synchronicity between the transitions and solar
464 forcing. The 100 realisations produced from our potential model, all initialised at the first
465 data point, appear broadly to follow the path of June insolation at 30°N with a small phase
466 lag (Figure 9). The model simulations also follow the speleothem palaeodata for all but the
467 monsoon transition at 129 ka BP near Termination II, where the model simulations show no

468 extended lag with respect to the insolation. Again it has to be kept in mind that the potential
469 model as a skeleton model can only be expected to qualitatively reproduce the main features
470 of the data. Actually observing the speleothem record as a realisation of the model will
471 always be highly unlikely with any model as simple as the present one.

472

473

474 **Figure 9** Probability range of 100 model simulations, with the June 30°N NHSI (in red),
475 and the palaeodata from SB11 (in green).

476

477

478 No consistent early warning signals were found in the initial 100 model simulations during
479 the period 224-128 kyr. In order to detect critical slowing down on the approach to a
480 bifurcation, the data must capture the gradual flattening of the potential well. We suggest
481 that early warning signals were not detected due to a relatively fast rate of forcing compared
482 to the sampling of the system; this comparatively poor sampling prevents the gradual
483 flattening of the potential well from being recorded in the data; a feature common to many
484 palaeoclimate datasets. Figure 10 illustrates the different flattening of the potential well
485 over a transition cycle during the glacial period and over the transition cycle at the
486 termination. There is more visible flattening in the potential at the termination, as seen in
487 panel (c), which is thought to be due to the reduced amplitude of the solar forcing at the
488 termination. The distinction between these two transitions cycles helps to explain why early
489 warning signals in the form of increasing autocorrelation and variance are found
490 immediately preceding the termination, but not for the other monsoon transitions.

491

492

493 **Figure 10** Potential analysis from the Sanabo $\delta^{18}\text{O}$ data showing the changing shape of the
494 potential well over (b) a transition cycle during the glacial period (198-175 kyr); and (c) the
495 transition cycle at the termination (150-128.5 kyr). Dotted lines show stages of the
496 transition over high, medium, and low insolation values, as depicted in panel (a).

497

498

499 To test the effect on the early warning signals of the sampling resolution of the model, we
500 compared a range of different sampling time steps in the model (see section 2.4) measuring
501 the Kendall tau values of autocorrelation and variance over each realisation of the model
502 (one realisation displayed in Figure 11), which demonstrates the effects of increasing the
503 sampling time step in the model. We found that whereas an increasing sampling time step
504 produces a steady decrease in the Kendall tau values for autocorrelation (Figure 11b),
505 Kendall tau values remain fairly constant for variance (Figure 11c), suggesting that the
506 latter is not affected by time step changes. This supports the contention by Dakos et al.
507 (2012b) that ‘high resolution sampling has no effect on the estimate of variance’. In
508 addition, we manipulated the noise level and found that decreasing the noise level by a
509 factor of 2 was necessary to identify consistent early warning signals. This is illustrated in
510 Figure 11a, where the grey line represents the noise level as determined by the model,
511 which does not follow a step transition, and cannot be adequately detrended by the equation
512 derived from the model. However, once the noise level is sufficiently reduced, early
513 warning signals (displayed here as high Kendall tau values for autocorrelation and variance)
514 can be detected.

515

516

517 **Figure 11** a) Example of single realisation of the approach to a bifurcation from our
518 potential model, which has been generated using 4 different noise levels (original noise =
519 grey, 0.5 noise = black, 0.2 noise = blue, 0.1 noise = green). Tipping point analysis was
520 applied on each realisation, where the red line depicts the detrending line and the grey
521 dashed vertical line is the cut-off point where data is analysed up to; distribution of Kendall
522 tau values for (a) autocorrelation and (b) variance over increasing sample step and differing
523 noise levels.

524

525

526 **4. Discussion**

527 It is important to note here that although the detection of early warning signals in time series
528 data has been widely used for the detection of bifurcations in a range of systems (Dakos et
529 al., 2008), there are instances when critical slowing down cannot be detected/recorded prior
530 to a bifurcation. First is the assumption that the abrupt monsoon shifts are characterised by a
531 bifurcation, rather than noise-induced tipping or stochastic resonance. The bifurcation
532 hypothesis is supported by previous studies (Zickfeld et al., 2005; Levermann et al., 2009;
533 Schewe et al., 2012) as well as our potential model, which selects a bifurcation as the most
534 likely scenario (whilst considering noise-induced tipping and stochastic resonance). In a
535 noise-induced tipping or stochastic resonance scenario, no early warning signals would be
536 expected since there would be no gradual change in the stability of the system (Lenton,
537 2011). Even within the bifurcation scenario, it is possible that early warning signals may not
538 be detected due to external dynamics of the system, such as a high level of stochastic noise,
539 or when there is an insufficient sampling resolution. The results illustrated in Figure 11
540 confirm that early warning signals may not be detected for bifurcations if the rate of forcing
541 is too fast compared to the sampling rate, such that the flattening of the potential is poorly

542 recorded in time series; Figure 11c clearly illustrates the detrimental effect of a lower
543 resolution on Kendall tau values, particularly for autocorrelation. ‘Missed alarms’ may
544 therefore be common in palaeodata where there is an insufficient sampling resolution to
545 detect the flattening of the potential; a high sampling resolution is thus recommended to
546 help avoid this issue. There is more flattening visible in the potential for the monsoon
547 transition at 129 ka BP (Termination II), which is due to the reduced amplitude of the
548 orbital forcing at the termination, but it is unclear whether this is sufficient to explain the
549 early warning signal detected in the palaeodata. We suggest that additional forcing
550 mechanisms may be driving the termination e.g. (Caley et al., 2011) which cannot be
551 captured by the potential model (as evidenced by the trajectory of the data falling outside
552 the probability range of the potential model (Figure 9)).

553

554 One possible reason for the detection of a critical slowing down immediately prior to the
555 termination (129 ka BP) is a change in the background state of the climate system.
556 Termination II is preceded by a Weak Monsoon Interval (WMI) in the EASM at 135.5-129
557 kyr (Cheng et al., 2009), characterised by the presence of a longer lag between the change
558 in insolation and the monsoon transition. The WMI is thought to be linked to migrations in
559 the Inter-tropical Convergence Zone (ITCZ) (Yancheva et al., 2007). Changes in the
560 latitudinal temperature gradient (Rind, 1998) or planetary wave patterns (Wunsch, 2006)
561 driven by continental ice volume (Cheng et al., 2009) and/or sea ice extent (Broccoli et al.,
562 2006) have been suggested to play a role in causing this shift in the ITCZ. For instance, the
563 cold anomaly associated with Heinrich event 11 (at 135 ka BP) has been invoked as a
564 possible cause of the WMI, cooling the North Atlantic and shifting the Polar Front and
565 Siberian High southwards, forcing an equatorward migration of westerly airflow across
566 Asia (Broecker et al., 1985; Cheng et al., 2009; Cai et al., 2015). Such a scenario would

567 have maintained a low thermal gradient between the land and sea, causing the Weak
568 Monsoon Interval and potentially suppressing a simple insolation response. The implication
569 is that during the earlier monsoon transitions in Stage 6, continental ice volume and/or sea-
570 ice extent was less extensive than during the WMI, allowing the solar insolation response to
571 dominate.

572

573

574 **5. Conclusions**

575 We analysed two speleothem $\delta^{18}\text{O}$ records from China over the penultimate glacial cycle as
576 proxies for the past strength of the EASM to test whether we could detect early warning
577 signals of the transitions between the strong and weak regimes. After determining that the
578 data was bimodal, we derived a non-stationary potential model directly from this data
579 featuring a fold bifurcation structure. We found evidence of critical slowing down before
580 the abrupt monsoon shift at Termination II (129 ka BP) in the speleothem $\delta^{18}\text{O}$ data.

581 However, we do not find consistent early warning signals of a bifurcation for the abrupt
582 monsoon shifts in the period between 224-150 kyr, which we term ‘missed alarms’.

583 Exploration of sampling resolution from our model suggests that the absence of robust
584 critical slowing down signals in the palaeodata is due to a combination of rapid forcing and
585 the insufficient sampling resolution, preventing the detection of the steady flattening of the
586 potential that occurs before a bifurcation. We also find that there is a noise threshold at
587 which early warning signals can no longer be detected. We suggest that the early warning
588 signal detected at Termination II in the palaeodata is likely due to the longer lag during the
589 Weak Monsoon Interval, linked to cooling in the North Atlantic. This allows a steadier
590 flattening of the potential associated with the stability of the EASM and thus enables the
591 detection of critical slowing down. Our results have important implications for identifying

592 early warning signals in other natural archives, including the importance of sampling
593 resolution and the background state of the climate system (full glacial versus termination).
594 In addition, it is advantageous to use archives which record multiple transitions, rather than
595 a single shift, such as the speleothem records reported here; the detection of an early
596 warning signal during one transition compared to previous events in the same record
597 provides an insight into changing/additional forcing mechanisms.

598

599

600

601 **References**

- 602 An, Z. et al. 2015. Global Monsoon Dynamics and Climate Change. *Annu. Rev. Earth*
603 *Planet. Sci.*, 43(2), pp.1–49.
- 604 An, Z. 2000. The history and variability of the East Asian paleomonsoon climate. *Quat. Sci.*
605 *Rev.*, 19(1-5), pp.171–187.
- 606 Ashwin, P. et al. 2012. Tipping points in open systems: bifurcation, noise-induced and rate-
607 dependent examples in the climate system. *Philos. Trans. R. Soc. A*, 370, pp.1166–
608 1184.
- 609 Baker, A.J. et al. 2015. Seasonality of westerly moisture transport in the East Asian
610 Summer Monsoon and its implications for interpreting precipitation $\delta^{18}\text{O}$. *J. Geophys.*
611 *Res. Atmos.*, p.n/a–n/a.
- 612 Berger, A. & Loutre, M.F. 1991. Insolation values for the climate of the last 10 million
613 years. *Quat. Sci. Rev.*, 10(1988), pp.297–317.
- 614 Boulton, C. A. & Lenton, T.M. 2015. Slowing down of North Pacific climate variability and
615 its implications for abrupt ecosystem change. *Proc. Natl. Acad. Sci.*, 2015,
616 p.201501781.
- 617 Broccoli, A.J., Dahl, K. a. & Stouffer, R.J. 2006. Response of the ITCZ to Northern
618 Hemisphere cooling. *Geophys. Res. Lett.*, 33, pp.1–4.
- 619 Broecker, W.S., Peteet, D.M. & Rind, D. 1985. Does the ocean-atmosphere system have
620 more than one stable mode of operation? *Nature*, 315, pp.21–26.
- 621 Cai, Y. et al. 2015. Variability of stalagmite-inferred Indian monsoon precipitation over the
622 past 252,000 y. *Proc. Natl. Acad. Sci.*, 112(10), pp.2954–2959.

- 623 Caley, T. et al. 2011. Orbital timing of the Indian, East Asian and African boreal monsoons
624 and the concept of a “global monsoon.” *Quat. Sci. Rev.*, 30(25-26), pp.3705–3715.
- 625 Cheng, H. et al. 2006. A penultimate glacial monsoon record from Hulu Cave and two-
626 phase glacial terminations. *Geology*, 34(3), p.217.
- 627 Cheng, H. et al. 2009. Ice Age Terminations. *Science (80-.)*, 326, pp.248–252.
- 628 Cheng, H. et al. 2012. The Global Paleomonsoon as seen through speleothem records from
629 Asia and the Americas. *Clim. Dyn.*, 39(5), pp.1045–1062.
- 630 Dakos, V. et al. 2012a. Methods for detecting early warnings of critical transitions in time
631 series illustrated using simulated ecological data. *PLoS One*, 7(7), p.e41010.
- 632 Dakos, V. et al. 2014. Resilience indicators: prospects and limitations for early warnings of
633 regime shifts. *Philos. Trans. R. Soc. B Biol. Sci.*, 370, p.20130263.
- 634 Dakos, V. et al. 2012b. Robustness of variance and autocorrelation as indicators of critical
635 slowing down. *Ecology*, 93(2), pp.264–271.
- 636 Dakos, V. et al. 2008. Slowing down as an early warning signal for abrupt climate change.
637 *Proc. Natl. Acad. Sci. U. S. A.*, 105(38), pp.14308–12.
- 638 Dansgaard, W. 1964. Stable isotopes in precipitation. *Tellus*, 4, pp.436–468.
- 639 Ditlevsen, P.D. & Johnsen, S.J. 2010. Tipping points: Early warning and wishful thinking.
640 *Geophys. Res. Lett.*, 37(19), p.L19703.
- 641 Donges, J.F. et al. 2015. Nonlinear regime shifts in Holocene Asian monsoon variability:
642 potential impacts on cultural change and migratory patterns. *Clim. Past*, 11, pp.709–
643 741.
- 644 Duan, F. et al. 2014. A high-resolution monsoon record of millennial-scale oscillations
645 during Late MIS 3 from Wulu Cave, south-west China. *J. Quat. Sci.*, 29(1), pp.83–90.
- 646 Hartigan, J.A. & Hartigan, P.M. 1985. The Dip Test of Unimodality. *Ann. Stat.*, 13(1),
647 pp.70–84.
- 648 Held, H. & Kleinen, T. 2004. Detection of climate system bifurcations by degenerate
649 fingerprinting. *Geophys. Res. Lett.*, 31(23), p.L23207.
- 650 Ives, A. 1995. Measuring Resilience in Stochastic Systems. *Ecol. Monogr.*, 65(2), pp.217–
651 233.
- 652 Kendall, M.G. 1948. *Rank correlation methods.*, Oxford: Griffen.
- 653 Kleinen, T., Held, H. & Petschel-Held, G. 2003. The potential role of spectral properties in
654 detecting thresholds in the Earth system: application to the thermohaline circulation.
655 *Ocean Dyn.*, 53(2), pp.53–63.
- 656 Kutzbach, J.E. 1981. Monsoon climate of the early Holocene: climate experiment with the
657 Earth’s orbital parameters for 9000 years ago. *Science (80-.)*, 214(4516), pp.59–61.

- 658 Kwasniok, F. 2015. Forecasting critical transitions using data-driven nonstationary
659 dynamical modeling. *Phys. Rev. E*, accepted.
- 660 Kwasniok, F. 2013. Predicting critical transitions in dynamical systems from time series
661 using nonstationary probability density modeling. *Phys. Rev. E*, 88, 052917.
- 662 Kwasniok, F. & Lohmann, G. 2009. Deriving dynamical models from paleoclimatic
663 records: Application to glacial millennial-scale climate variability. *Phys. Rev. E*, 80(6),
664 066104.
- 665 Lee, J.-E. & Swann, A.L. 2010. Evaluation of the “amount effect” at speleothem sites in the
666 Asian monsoon region. *IOP Conf. Ser. Earth Environ. Sci.*, 9, p.012023.
- 667 Lenton, T.M. 2011. Early warning of climate tipping points. *Nat. Clim. Chang.*, 1(4),
668 pp.201–209.
- 669 Lenton, T.M. et al. 2012. Early warning of climate tipping points from critical slowing
670 down: comparing methods to improve robustness. *Philos. Trans. R. Soc. A Math. Phys.*
671 *Eng. Sci.*, 370(1962), pp.1185–1204.
- 672 Levermann, A. et al. 2009. Basic mechanism for abrupt monsoon transitions. *Proc. Natl.*
673 *Acad. Sci. U. S. A.*, 106(49), pp.20572–7.
- 674 Li, T.-Y. et al. 2013. Variability of the Asian summer monsoon during the penultimate
675 glacial/interglacial period inferred from stalagmite oxygen isotope records from
676 Yangkou cave, Chongqing, Southwestern China. *Clim. Past Discuss.*, 9(6), pp.6287–
677 6309.
- 678 Lisiecki, L.E. & Raymo, M.E. 2005. A Pliocene-Pleistocene stack of 57 globally distributed
679 benthic $\delta^{18}\text{O}$ records. *Paleoceanography*, 20(1), pp.1–17.
- 680 Liu, X. et al. 2006. Hemispheric Insolation Forcing of the Indian Ocean and Asian
681 Monsoon: Local versus Remote Impacts. *Am. Meteorol. Soc.*, 19, pp.6195–6208.
- 682 Liu, Z. et al. 2014. Chinese cave records and the East Asia Summer Monsoon. *Quat. Sci.*
683 *Rev.*, 83, pp.115–128.
- 684 Maher, B.A. 2008. Holocene variability of the East Asian summer monsoon from Chinese
685 cave records: a re-assessment. *The Holocene*, 18(6), pp.861–866.
- 686 Pausata, F.S.R. et al. 2011. Chinese stalagmite $\delta^{18}\text{O}$ controlled by changes in the Indian
687 monsoon during a simulated Heinrich event. *Nat. Geosci.*, 4(7), pp.474–480.
- 688 Petit, J.R. et al. 1999. Climate and atmospheric history of the past 420,000 years from the
689 Vostok ice core, Antarctica. *Nature*, 399, pp.429–436.
- 690 Rind, D. 1998. Latitudinal temperature gradients and climate change. *J. Geophys. Res.*, 103,
691 p.5943.
- 692 Rodionov, S.N. 2004. A sequential algorithm for testing climate regime shifts. *Geophys.*

693 *Res. Lett.*, 31(9), p.L09204.

694 Ruddiman, W.F. 2006. What is the timing of orbital-scale monsoon changes? *Quat. Sci.*
695 *Rev.*, 25(7-8), pp.657–658.

696 Scheffer, M. 2010. Foreseeing tipping points. *Nature*, 467, pp.6–7.

697 Schewe, J., Levermann, A. & Cheng, H. 2012. A critical humidity threshold for monsoon
698 transitions. *Clim. Past*, 8(2), pp.535–544.

699 Sun, Y. et al. 2015. Astronomical and glacial forcing of East Asian summer monsoon
700 variability. *Quat. Sci. Rev.*, 115(2015), pp.132–142.

701 Thompson, J. & Sieber, J. 2011. Predicting climate tipping as a noisy bifurcation: a review.
702 *Int. J. Bifurc. Chaos*, 21(2), pp.399–423.

703 Wang, H. & Chen, H. 2012. Climate control for southeastern China moisture and
704 precipitation: Indian or East Asian monsoon? *J. Geophys. Res. Atmos.*, 117(D12),
705 p.D12109.

706 Wang, Y. et al. 2008. Millennial- and orbital-scale changes in the East Asian monsoon over
707 the past 224,000 years. *Nature*, 451, pp.18–21.

708 Wang, Y. et al. 2009. Sanbao Cave, China 224 KYr Stalagmite d¹⁸O Data. IGBP
709 PAGES/World Data Center for Paleoclimatology Data Contribution Series # 2009-
710 138. NOAA/NCDC Paleoclimatology Program, Boulder CO, USA.

711 Wang, Y.J. et al. 2001. A high-resolution absolute-dated late Pleistocene Monsoon record
712 from Hulu Cave, China. *Science (80-.)*, 294(5550), pp.2345–8.

713 Wu, G. et al. 2012. Thermal controls on the Asian summer monsoon. *Sci. Rep.*, 2(404),
714 pp.1–7.

715 Wunsch, C. 2006. Abrupt climate change: An alternative view. *Quat. Res.*, 65(2006),
716 pp.191–203.

717 Yancheva, G. et al. 2007. Influence of the intertropical convergence zone on the East Asian
718 monsoon. *Nature*, 445(7123), pp.74–7.

719 Yuan, D. et al. 2004. Timing, duration, and transitions of the last interglacial Asian
720 monsoon. *Science (80-.)*, 304(5670), pp.575–8.

721 Zhang, P. et al. 2008. A test of climate, sun, and culture relationships from an 1810-year
722 Chinese cave record. *Science (80-.)*, 322(5903), pp.940–2.

723 Zickfeld, K. et al. 2005. Is the Indian summer monsoon stable against global change?
724 *Geophys. Res. Lett.*, 32(15), p.L15707.

725

726

727 **Acknowledgements**

728 We thank Sue Rouillard from the drawing office in the Geography department at the

729 University of Exeter for drawing Figure 2.

730 The data for this paper are available from the National Climate Data Centre, NOAA (SB11:

731 http://hurricane.ncdc.noaa.gov/pls/paleox/f?p=519:1:::P1_STUDY_ID:8641 and Hulu:

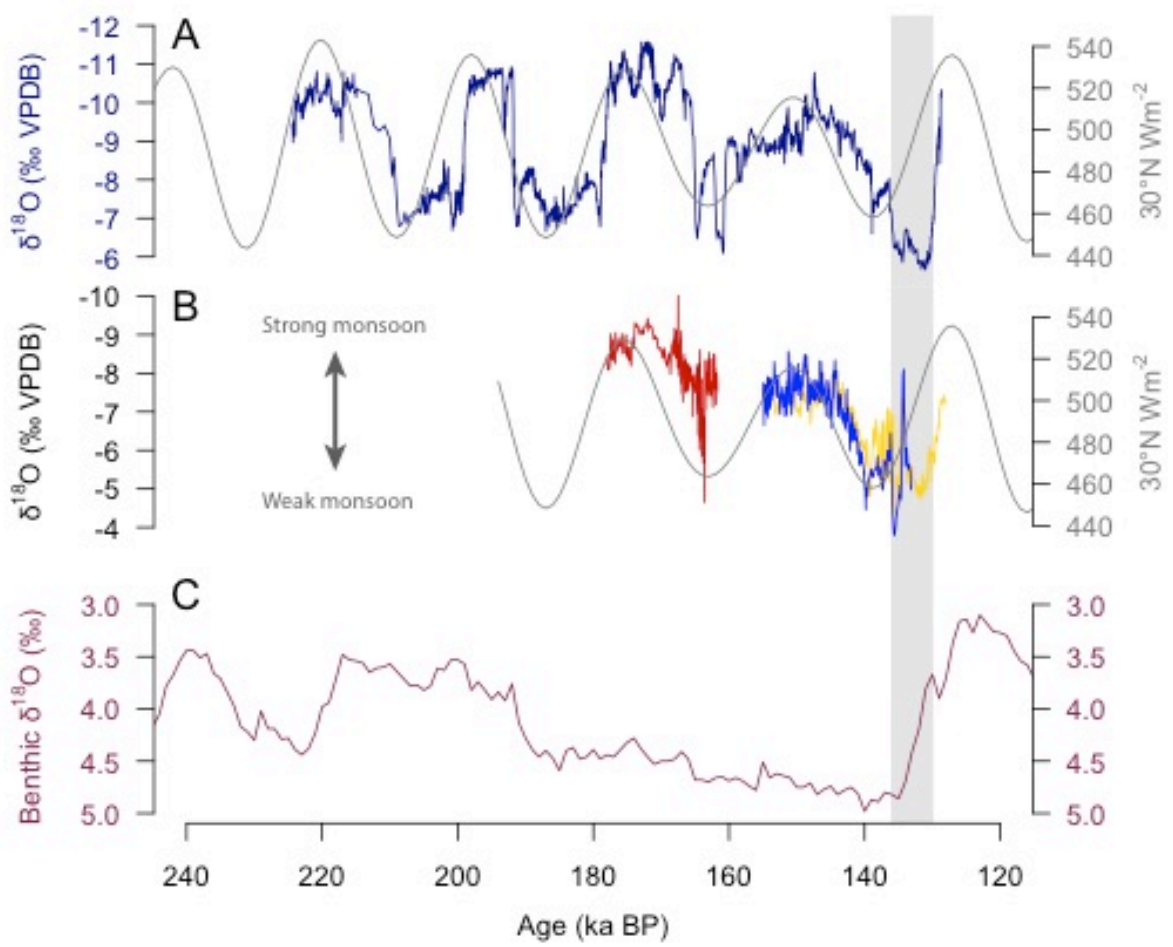
732 http://hurricane.ncdc.noaa.gov/pls/paleox/f?p=519:1:::P1_STUDY_ID:5426)

733

734 **Competing financial interests**

735 The authors declare no competing financial interests.

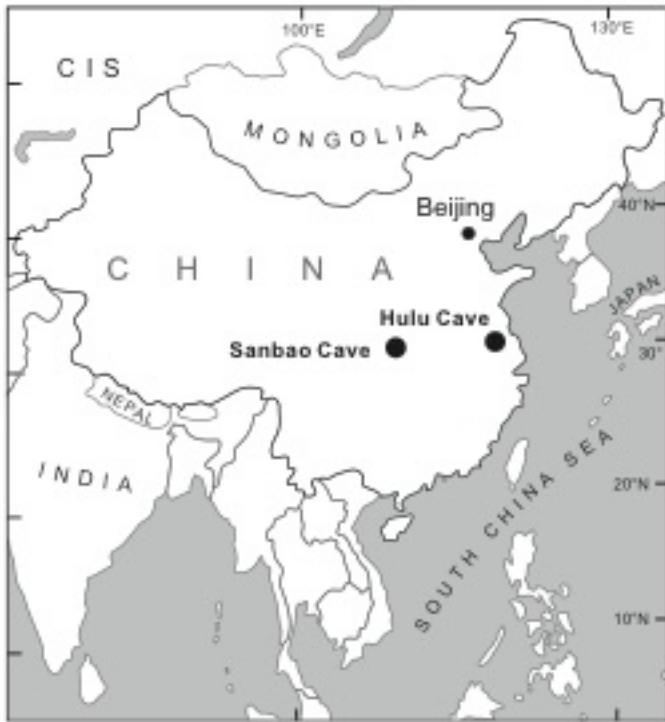
736



737

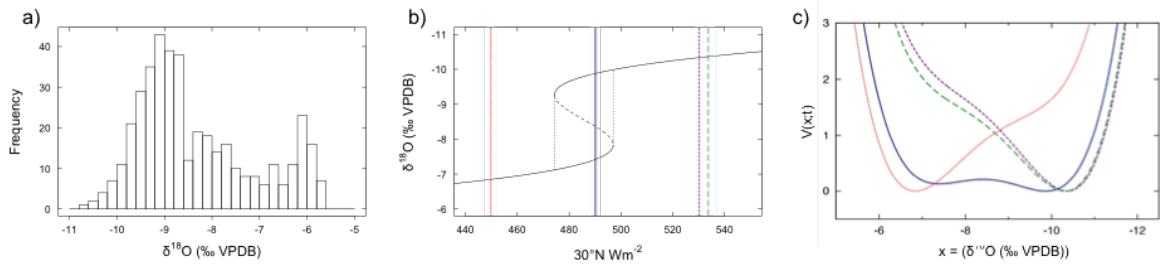
738

739 Figure 1



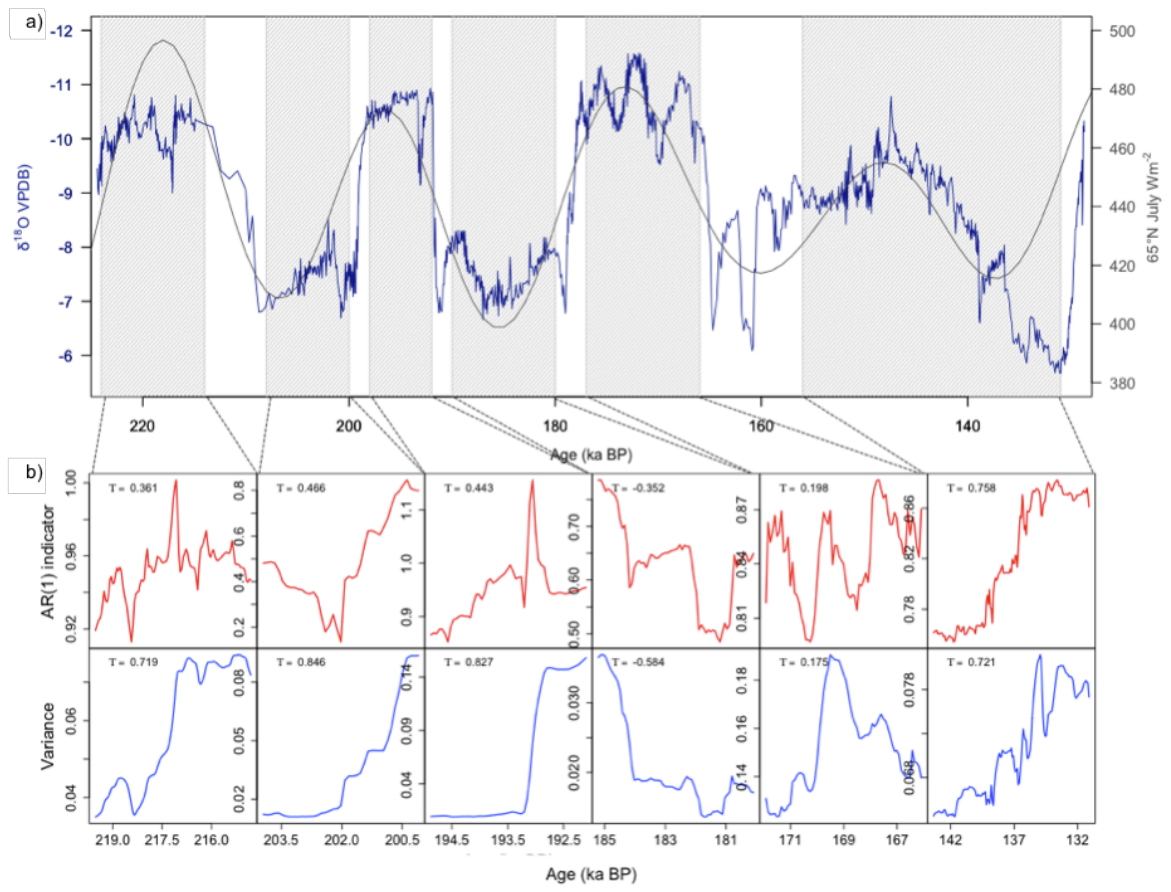
740

741 Figure 2



742

743 Figure 3



744

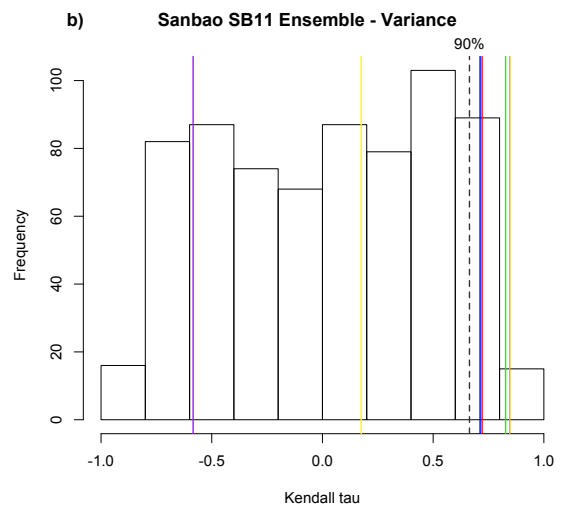
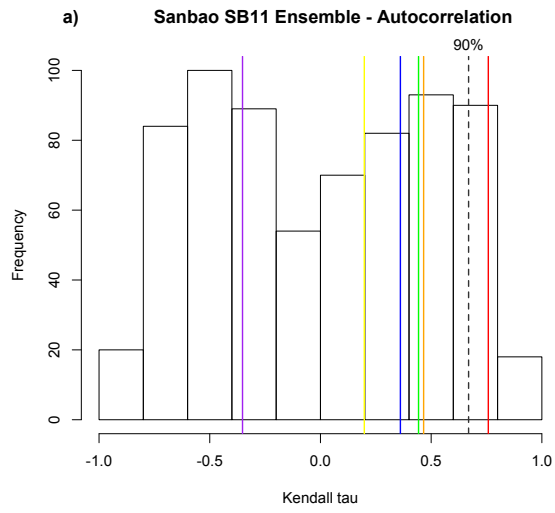
745 Figure 4

746

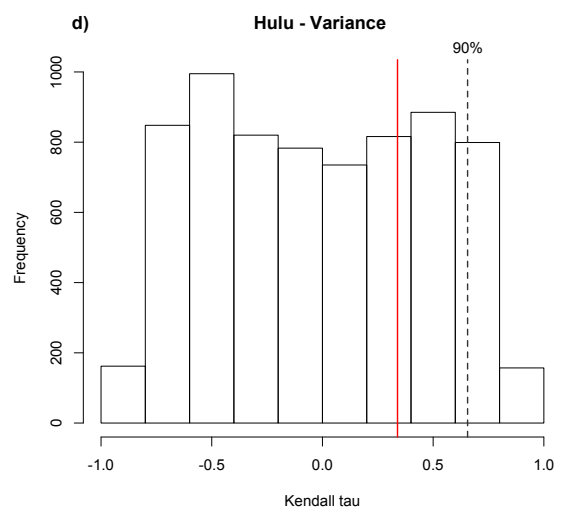
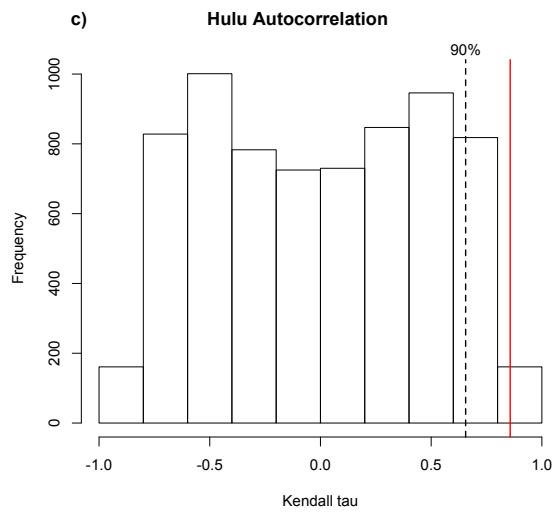
747

748

749



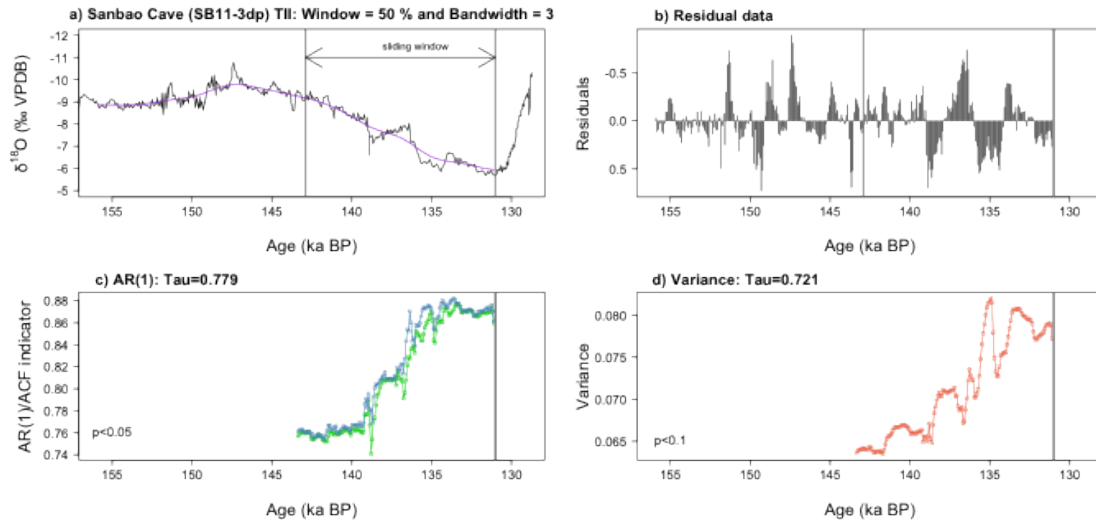
750



751

752 Figure 5

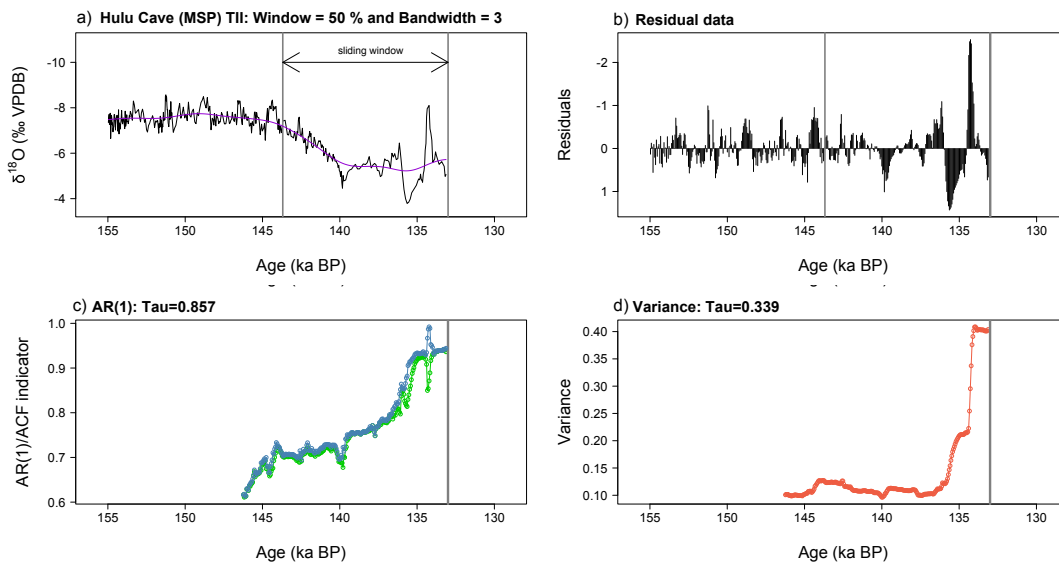
753



754

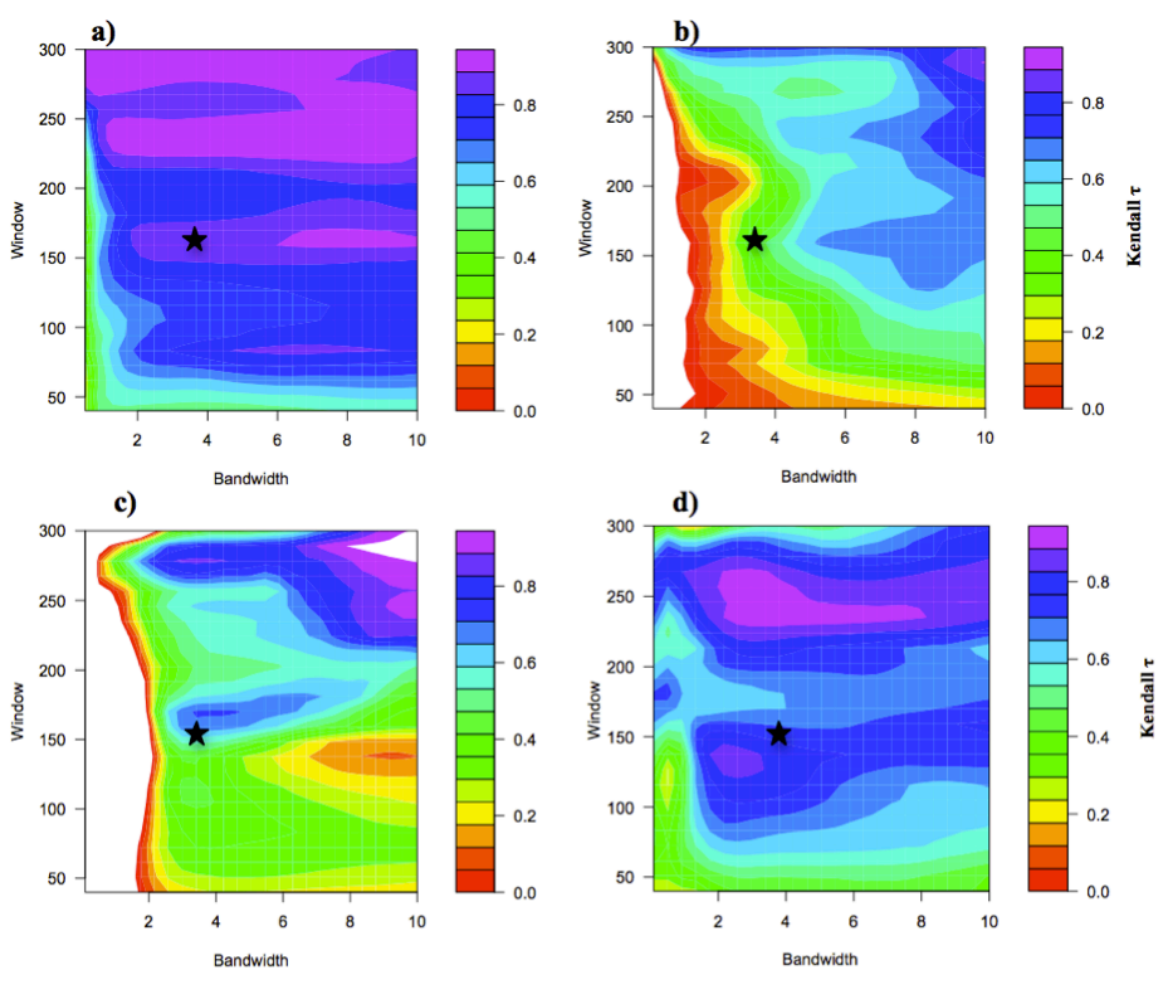
755 Figure 6

756



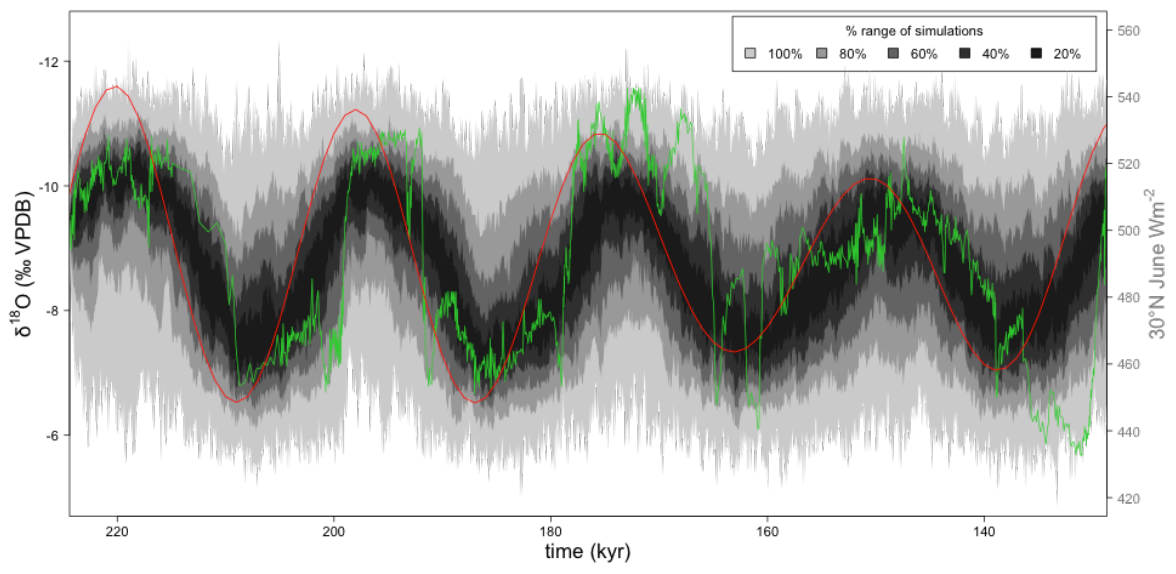
757

758 Figure 7



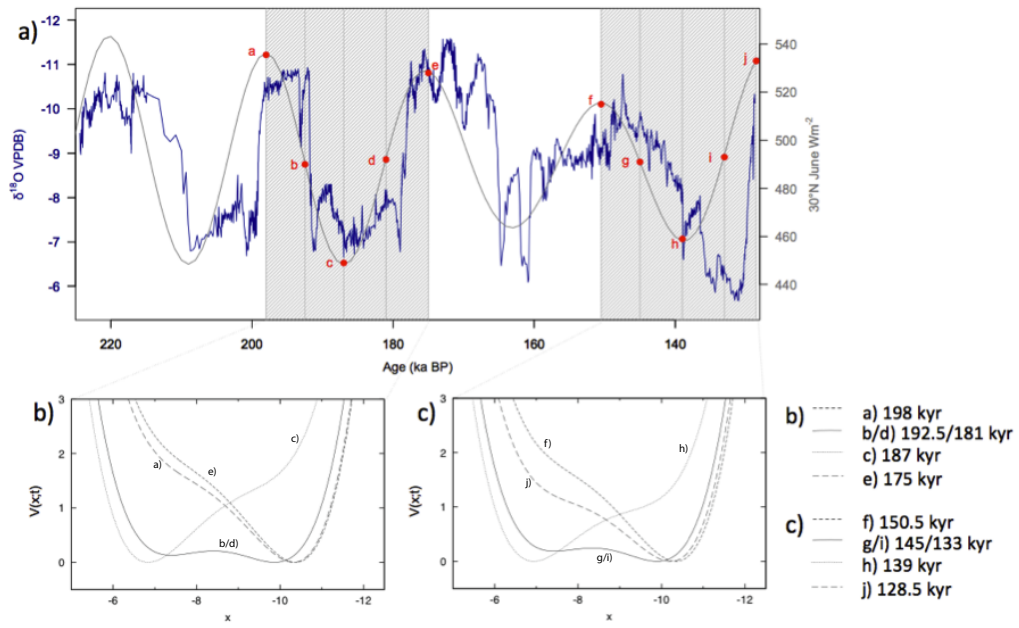
759

760 Figure 8



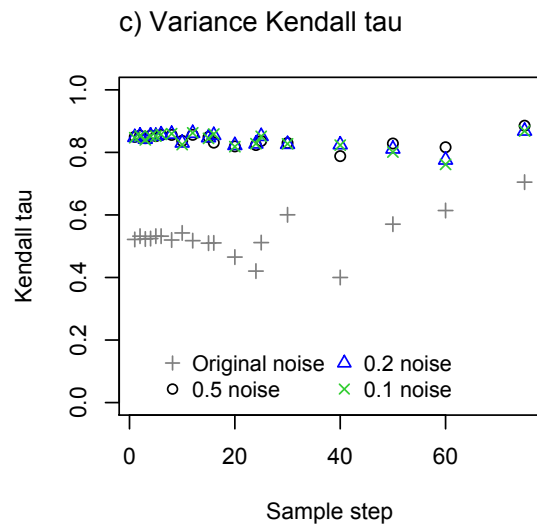
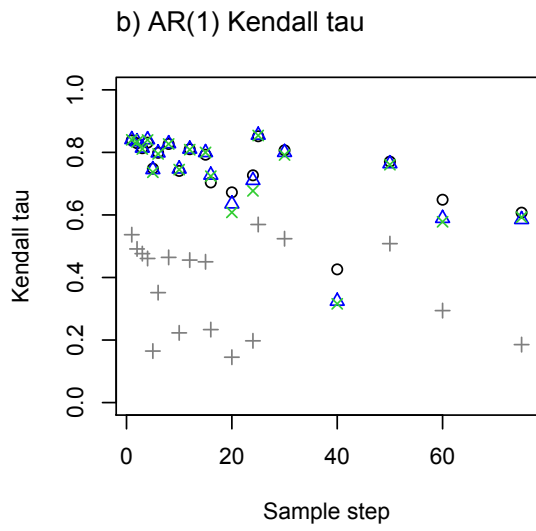
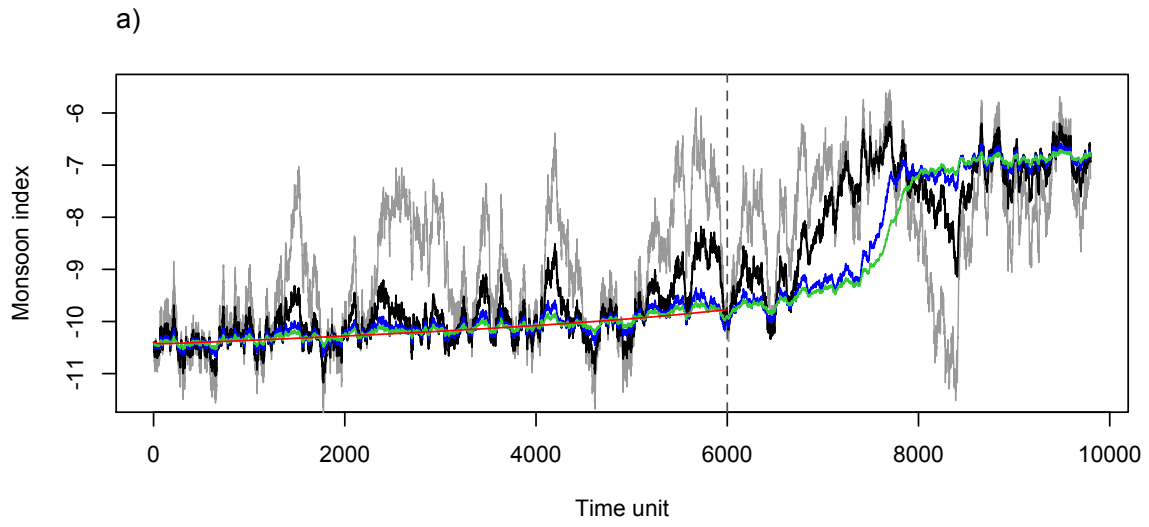
761

762 Figure 9



763

764 Figure 10



765

766 Figure 11

767

768

769

770

771